Contributions to the 6th AIAA CFD Drag Prediction Workshop Using Structured, Overset Grid Methods

James G. Coder[1]
University of Tennessee, Knoxville, TN, 37996

David Hue[2]
ONERA, the French Aerospace Lab, 92190 Meudon, France

Gaetan Kenway[3]
University of Michigan, Ann Arbor, MI, 48109

Thomas H. Pulliam[4]
NASA Ames Research Center, Moffett Field, CA, 94035

and

Anthony J. Sclafani[5]
Boeing Commercial Airplanes, Long Beach, CA, 90808

Structured-grid solutions obtained for the NASA Common Research Model for the 6th AIAA CFD Drag Prediction Workshop are detailed. Three different flow solvers were used amongst the contributors: OVERFLOW, ADflow, and elsA. The numerical methodologies and turbulence modeling strategies employed by each code are described. Key results for all authors include grid convergence studies for the drag increment of a nacelle and pylon added to a wing-body configuration and a buffet study accounting for static aeroelastic deformation. Additional studies performed include feature-based adaptive mesh refinement and higher-order convective flux discretization, among others.

Nomenclature

AR	=	wing aspect ratio
b	=	span
C_p	=	pressure coefficient
C_D	=	drag coefficient
C_L	=	lift coefficient
C_M	=	pitching-moment coefficient
c	=	chord
c_d	=	section profile-drag coefficient
c_l	=	section lift coefficient
c_m	=	section pitching-moment coefficient about the quarter chord
M	=	Mach number
N	=	total number of grid points
Re	=	Reynolds number based on reference chord length

---

[1] Assistant Professor, Dept. of Mechanical, Aerospace and Biomedical Engineering, Senior Member AIAA.
[2] Engineer, Applied Aerodynamics Department, Member AIAA.
[3] Postdoctoral Research Fellow, Dept. of Aerospace Engineering, Member AIAA.
[4] Research Scientist, Associate Fellow AIAA.
[5] Aerodynamics Engineer, Senior Member AIAA.

S	=	reference wing area
x	=	x-coordinate direction
y	=	y-coordinate direction
α	=	angle of attack
η	=	non-dimensional spanwise coordinate, $2y/b$
Subscripts		
∞	=	free-stream conditions

I. Introduction

THE AIAA Drag Prediction Workshop (DPW) series was first organized to assess the state-of-the-art in computational fluid dynamics (CFD) methods for predicting aircraft forces and moments, to provide a forum for evaluating the effectiveness of codes and modeling techniques, and identify areas for improvement. The first DPW was held in Anaheim, CA in 2001, and the 6th and most recent workshop was held in June 2016 in conjunction with the 34th AIAA Applied Aerodynamics Conference in Washington, DC.

The focus of the 6th Drag Prediction Workshop (DPW-6)[1] is the Common Research Model (CRM), pictured in Fig. 1, which was designed in cooperation by Boeing and NASA to be an open-source commercial transport configuration.[2] The CRM was also used for the 4th and 5th Drag Prediction Workshops[3,4] in 2009 and 2012, respectively. In DPW-4, participant simulations of the CRM wing-body-tail were performed 'blind' and pre-dated the availability of experimental, wind-tunnel force and moment measurements. By DPW-5, experimental data for a 2.7% scale model were available from the NASA Langley NTF and the NASA Ames Transonic Wind Tunnel[5]; however, it was discovered that the test article was fabricated to have 1-g deformed wing shape when the model was unloaded. During the experiments, the wing experienced additional aero-elastic deflection and twist, thereby causing a discrepancy between what was tested and what was simulated. The deflections and twists of the experiment were measured and are the basis for a revised CAD definition of the CRM for DPW-6.

Test cases for DPW-6 included a grid-convergence study for the drag increment between the wing-body (WB) and wing-body-nacelle-pylon (WBNP) configurations, an angle-of-attack sweep using grids based on the measured aero-elastic deflections, a grid-adaptation study, and a coupled aero-elastic simulation. An additional turbulence model verification study was also included. Participants of DPW-6 employed a wide range of solver methodologies, such as structured overset, unstructured finite volume, unstructured finite element, and lattice Boltzmann. The structured, overset contributions to the workshop are documented herein, and include submissions using three codes from four teams encompassing five organizations: Boeing/NASA, the Penn State University Applied Research Laboratory, the University of Michigan, and ONERA.
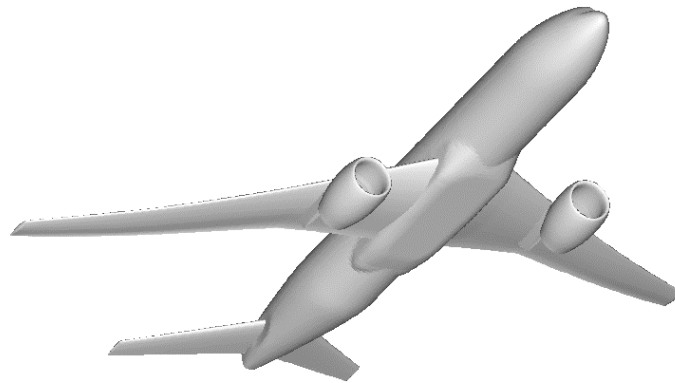

Figure 1. CRM WBTNP configuration (from Ref. 2).

II. Description of DPW-6 Geometry and Cases

The CRM is intended to be representative of modern wide-body commercial transports. Its wing planform is shown in Fig. 2, and its key geometric parameters are summarized in Table 1.
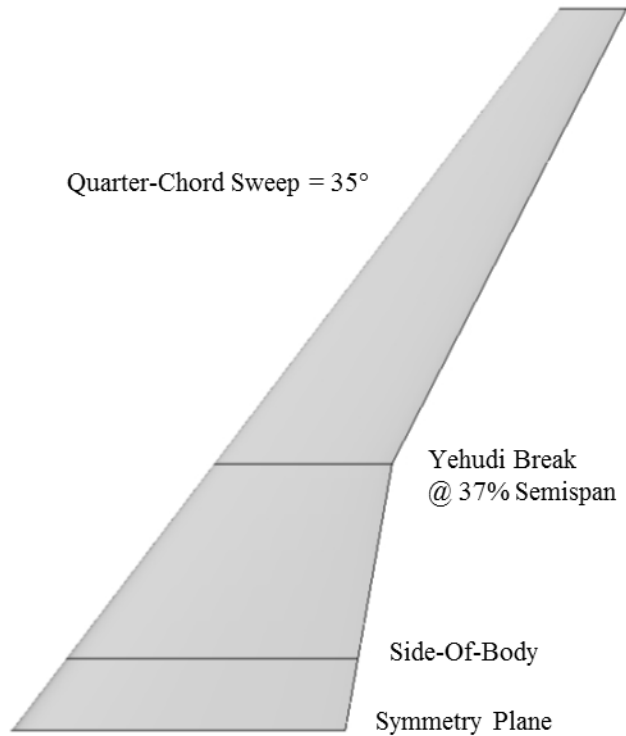
Figure 2. CRM wing planform.[2]

Table 1. CRM wing geometric reference parameters.[2]

Wing Reference Area, S_{ref}	594,720.0 in^2
Trap-Wing Area	576,000 in^2
Reference Chord, c_{ref}	275.80 in
Span, b	2313.50 in
Taper Ratio, λ	0.275
Quarter-Chord Sweep, $\Lambda_{c/4}$	35°
Aspect Ratio, AR	9.0

The test matrix for DPW-6 includes a two-dimensional turbulence model verification study from the NASA Turbulence Modeling resource[6], a grid-convergence study of the nacelle-pylon drag increment, a wing-body buffet study (angle-of-attack sweep) using the measured aero-elastic deformations, a grid-adaptation study using the wing-body geometry, and a coupled aero-structural simulation of the wing-body. All CRM simulations are specified to be in free air with a free-stream Mach number of 0.85, a Reynolds number of 5 million based on the mean aerodynamic chord, and a reference temperature of 100°F. These cases are summarized in Table 2 below.

Table 2. DPW-6 case definitions.

Case	Conditions	Description
Case 1: Verification Study (NACA 0012 airfoil)	M = 0.15, Re = 6 x 10^6, α = 10°	Grid convergence study using NACA 0012 grid family from NASA TMR website[6]
Case 2: CRM Nacelle-Pylon Drag Increment	M = 0.85, Re = 5 x 10^6, C_L = 0.5 +/- 0.0001	Grid convergence studies for the WB and WBNP geometries using α = 2.75° (C_L = 0.5) measured aero-elastic deflections
Case 3: CRM WB Static Aero-Elastic Effect	M = 0.85, Re = 5 x 10^6, α = [2.50, 2.75, 3.00, 3.25, 3.50, 3.75, 4.00] degrees	Angle-of-attack sweep for the WB geometry using measured aero-elastic deflections for each angle
Case 4: CRM WB Grid	M = 0.85, Re = 5 x 10^6,	Participant-generated adapted grid family

American Institute of Aeronautics and Astronautics

Adaptation	C_L = 0.5 +/- 0.0001	starting from Tiny or Coarse baseline mesh and α = 2.75° aero-elastic deflection
Case 5: CRM WB Coupled Aero-Structural Simulation	M = 0.85, Re = 5 x 10^6, C_L = 0.5 +/- 0.0001	Coupled CFD/CSD simulation using medium-resolution grid and provided FEM model and mode shapes

III. Numerical Methodologies

A. Solver Descriptions
1. OVERFLOW

OVERFLOW 2.2[7] is a widely used RANS computational fluid dynamics code considered reliable and accurate for analyzing modern transport configurations, like the CRM, at or near the cruise design condition. Originally developed by NASA with numerous contributions from academia and industry, it is a node-based solver specifically designed for structured overset grids where many options are available to the user such as 2D/3D and steady/unsteady simulations, thin-layer vs. full Navier-Stokes, quadratic constitutive relation (QCR)[8], and multiple turbulence models. While the flow regime and geometry of interest narrows-down the solver options, there are still many combinations of numerical schemes, dissipation parameters and turbulence models to pick from. The settings applied to the CRM test case are provided for reference.

Two sources of OVERFLOW data were presented at DPW-6. The first came from Pulliam and Sclafani, who ran cases on the NASA Pleiades supercomputer, and the second from Coder, who utilized computing resources at the Pennsylvania State University Applied Research Laboratory. For the Pleiades runs, version 2.2k was used with a setup consistent with the CRM analysis from DPW-5[9] with the full Navier-Stokes option (as opposed to thin-layer mode), second-order central differencing with matrix dissipation for convection terms, the implicit ARC3D diagonalized scalar pentadiagonal scheme for solution advancement, the "noft2" version of the Spalart-Allmaras one-equation turbulence model[10] with rotation and curvature corrections[11] turned-on, an exact wall distance calculation, and multi-grid convergence acceleration. All cases were run in a non-time accurate mode (e.g. full-multigrid, spatially varying time steps). The effect of QCR was investigated in this analysis.

For the second source of OVERFLOW data, from ARL Penn State, version 2.2l was used to evaluate benefits of using higher-order convective fluxes on a cruise configuration such as the CRM. Fifth-order WENO and third-order MUSCL schemes with Roe fluxes were used for spatial discretization. To accelerate convergence, all solutions were initialized by using with the 3rd-order MUSCL discretization and the implicit, ARC3D scalar pentadiagonal solver for first 5000 iterations. Afterwards, the left-hand side was switched to the robust SSOR scheme available in OVERFLOW, which requires no artificial dissipation but did not permit multi-grid acceleration. For the WENO solutions the spatial discretization was switched at this point as well. The Spalart-Allmaras model with the rotation/curvature corrections and QCR was also employed.

2. elsA

The structured-grid solver elsA is a cell-centered, finite volume, RANS code originally developed by ONERA and capable of using both point-matched and overset grids. For the DPW-6 studies, an implicit LU-SSOR solver was used with a backward-Euler time discretization with the 2nd-order central differencing scheme of Jameson[12]. Turbulence was modeled with the one-equation Spalart-Allmaras eddy-viscosity model either with or without a quadratic constitutive relation. One level of multigrid was employed to accelerate solution convergence. Overset interpolations used two fringe layers and special treatment of solid surfaces defined by multiple overlapping meshes. Solution convergence was regarded as occurring when the lift coefficient variation was within +/- 0.001 and drag coefficient was within 0.00005 for the previous 1000 iterations. More detail on the ONERA simulations for DPW-6 may be found in Ref. 13.

3. ADflow

ADflow is a finite-volume RANS code maintained by the Multidisciplinary Design Optimization Laboratory (MDOlab) at the University of Michigan. ADflow was originally developed as SUmb[14], which is a multiblock solver for the RANS, laminar Navier-Stokes, or Euler equations in either steady, unsteady, or time-spectral modes[14,15]. The MDOlab developed a discrete adjoint method that efficiently computes the derivatives of force coefficients with respect to shape variables[16], enabling ADflow to be used for aerodynamic[17,18,19,20] and aerostructural[21,22] aircraft design optimization.

As with most CFD solvers, several discretization schemes and turbulence models are available. For the ADflow results contained in this paper, the scalar artificial dissipation scheme of Jameson[12] is employed throughout. The viscous flux gradients are computed using the Green-Gauss approach. The Spalart-Allmaras turbulence model is used unless otherwise noted. A fully-coupled Newton-Krylov method is used to solve the mean flow and turbulence equations simultaneously, yielding a robust method with rapid convergence near the solution.

More recently, a chimera overset grid method was implemented in ADflow. For the chimera approach, all interpolation and blanking information is computed internally using an efficient and parallelized preprocessing module. The method closely follows the implicit hole cutting method described by Landmann and Montagnac[23]. This method is automatic and requires no additional user input other than the computational blocks and their associated boundary conditions. The implicit hole cutting approach was able to successfully compute overset grid connectivity for all wing-body and wing-body-nacelle-pylon configurations presented herein with no resulting orphan cells.

The force and moment integrations use the zipper mesh approach described by Chan[24].

B. Grid Systems

1. Standard Overset Grid System

The overset grid families for the CRM WB and WBNP aero-elastic configurations were generated by Leonel Serrano and Dr. John Vassberg at Boeing. A new grid generation process was established for this workshop where the gridding guidelines were followed as closely as possible by starting with the coarsest grid level and refining to the next denser mesh using a factor of 1.5 on the total number of points. Considering grid dimensions in each of the three directions, the cube root of 1.5 is approximately 1.14 (i.e., 8/7) so this factor was used to guide the selection of point numbers along with the requirement of being multi-grid friendly to at least three levels. In order to ensure the guidelines were met, a unique set of factors were applied to each grid level per Table 3 below. Note that N in this table is an even integer.

Table 3. Overset Grid Family Factors.

Level	Cell Dim	Growth Factor
Tiny	4 x N	
		$(5/4)^3 = 1.953$
Coarse	5 x N	
		$(6/5)^3 = 1.728$
Medium	6 x N	
		$(7/6)^3 = 1.588$
Fine	7 x N	
		$(8/7)^3 = 1.493$
eXtra-Fine	8 x N	
		$(9/8)^3 = 1.125$
Ultra-Fine	9 x N	

The above table shows that the target ratio of 8/7 was met as the Fine grid was refined to the Extra-Fine grid where the growth factor was 1.493. The table also shows how the growth factor on total number of points monotonically decreases starting with 1.953 for the Tiny-to-Coarse refinement.

The process used to generate the overset grid families is based on the ICEMCFD HEXA software package[25] where surface grids were built directly on the CAD geometry using a "blocking file" approach. This process allows for some degree of automation by applying the same set of parameters to each grid in the family. The resulting grid system for a given level is made up of a consistent set of zones with the exact same topology applied to the exact same surface definition. The surface grids were then used to build volume grids using NASA's Chimera Grid Tools (CGT) package[26] coupled with a NASA tcl script system which defines boundary conditions for each zone, organizes components with a master configuration file, and drives the CGT programs with a master input file. A script tool called BuildVol generates volume grids where surface grids are run through one of two hyperbolic grid generators (HYPGEN and LEGRID) and Cartesian box grids are created using BOXGR. Grid connectivity was

accomplished using PEGASUS5. The resulting system of volume grids are summarized in Table 4. Note that the total number of points shown in this table includes those with an iblank value of 0 (i.e., hole points).

Table 4. CRM WB and WBNP Overset Grid Information.

level	viscous spacing (in)	~y+	# of const. cells at wall	max. stretching	Total Number of Points WB	Total Number of Points WBNP
Tiny	0.001478	1.02	4	1.235	7,398,176	11,865,177
Coarse	0.001182	0.80	5	1.186	14,355,678	22,999,565
Medium	0.0009853	0.67	5	1.149	24,698,828	39,542,953
Fine	0.0008446	0.58	6	1.128	39,098,858	62,566,221
X-fine	0.0007390	0.50	7	1.112	58,227,000	93,176,522
U-fine	0.0006569	0.45	8	1.099	82,754,486	132,381,764

Figure 3 compares surface grid density for the WBNP overset grid family. The WB grids were created by simply removing the NP group and re-running PEGASUS5, so the grid point clustering on the wing behind the nacelle remained in the WB grid system. This resulted in a very consistent set of grids for the NP incremental study.
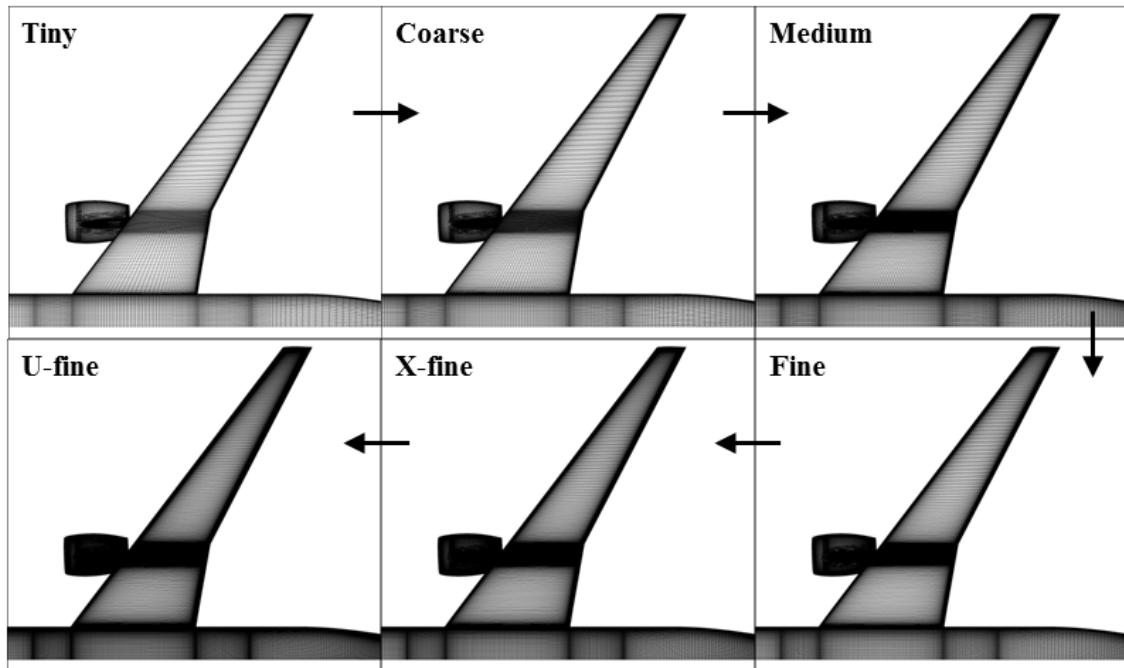

Figure 3. CRM WBNP Surface Grid Density Variation.

2. UM Modified Overset Grid System

Although the Standard Overset grid system was generated to provided sufficient overlap of the grids for a node-centered overset solver; however, this overlap was found to be insufficient for the cell-centered ADflow solver. This necessitated a regeneration of the volume meshes to ensure positive volumes, creating a Modified Overset grid system. New volume grids were generated based on the near-field surface meshes of the standard overset system. All near-field meshes in the Modified Overset system are identical to the Standard Overset meshes, with the exception of the nacelle body grid. It was modified to provide slightly more overlap near the front of the nacelle for coarser meshes. The full mesh refinement series (Tiny through XFine) use this modification, and the number of

American Institute of Aeronautics and Astronautics

nodes and spacings are kept consistent with the Standard Overset grids. A comparison of the two Tiny surface meshes are shown in Fig. 4. The near-field volume meshes were extruded using an in-house hyperbolic mesh generator. The number of nodes, marching distance, and stretching ratios were kept close to the Standard Overset grids; however, due to the use of a different grid-generation algorithm, the resulting volume meshes differ slightly. A comparison of several slices of the Tiny mesh is depicted in Fig. 5. Finally, the Standard Overset background meshes were utilized with one exception: the two Cartesian blocks at the leading and trailing edge of the nacelle were merged to create a single block covering the entire nacelle region. This modification is shown in Fig. 6.

An additional, point-matched multiblock was generated for use with the ADflow solver. These grids were generated based on the same meshing guidelines as the Standard and Modified Overset grid systems. A key difference in the grids, as will be highlighted later in the results section, is that the mesh topology in the wing-body juncture differs. The differences are pictured in Fig. 7. In the overset grid systems, the wing-body collar grid (Fig. 7a) has all viscous surfaces on the same computational plane. Consequently, there is skew in the grid lines as they extrude outward. In the multiblock system (Fig. 7b), the wing and the body surfaces are separate computational planes, leading to a grid that is more orthogonal.
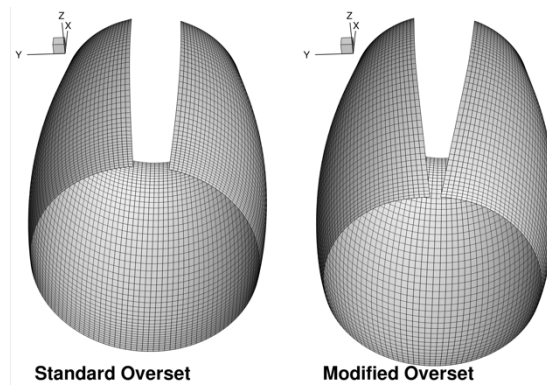

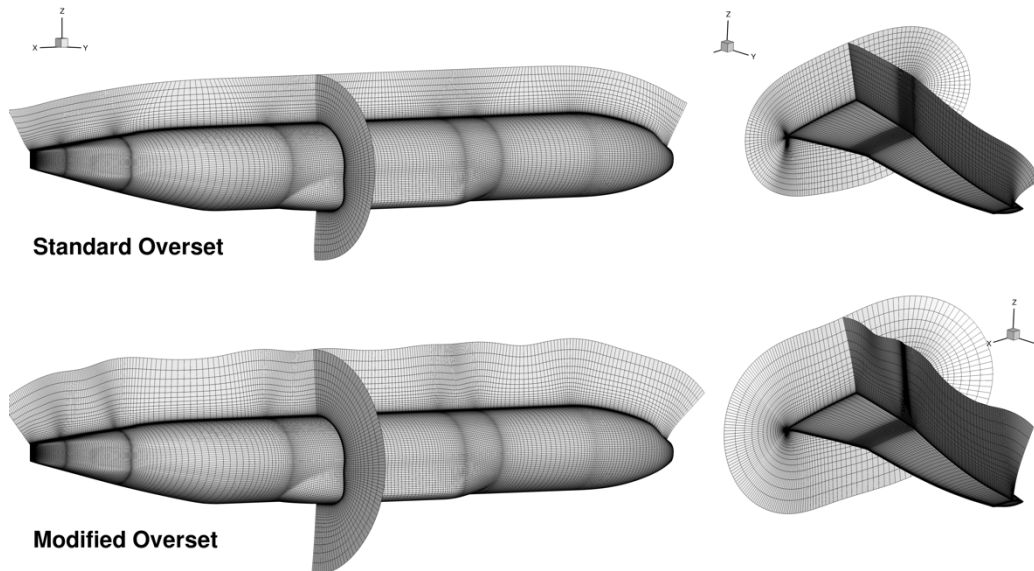**Figure 4. Modification of nacelle surface mesh**

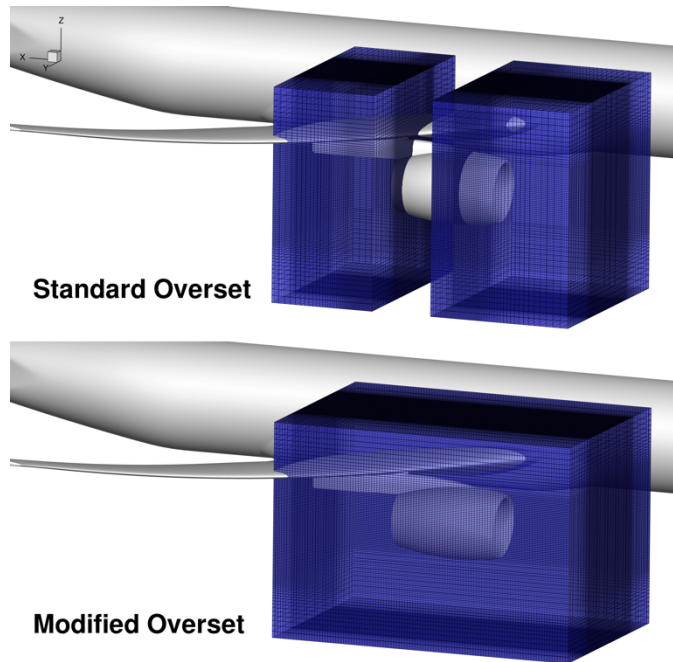**Figure 5. Comparison of Standard Overset and Modified Overset body-fitted volume meshes.**

American Institute of Aeronautics and Astronautics

Figure 6. Revised nacelle-pylon refinement block.
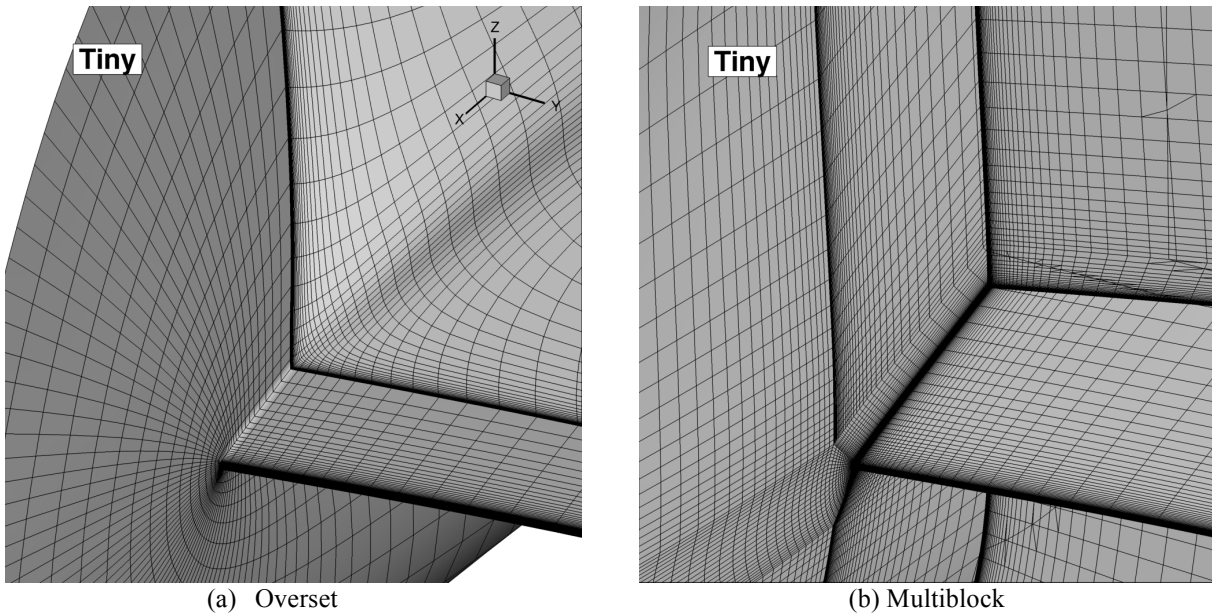

(a) Overset   (b) Multiblock

Figure 7. Grid topology differences in wing-body juncture.

C. Turbulence Closure

All CFD codes used for the results presented in this work solve the Reynolds-averaged Navier-Stokes (RANS) equations, which requires additional closure relations to define the turbulent stress tensor. To this end, all results in this paper were obtained using the one-equation, Spalart-Allmaras (SA) model[10]. This model is rooted in the Boussinesq approximation and uses a field PDE to solve for the eddy viscosity. Additional features/capabilities of the SA model were also employed, such as the Spalart-Shur streamline rotation/curvature correction[11] and a quadratic constitutive relation[8]. The use of the rotation/curvature correction, termed the "SA-RC" variant, improves the model's prediction around leading edges and in vortex cores. The quadratic constitutive relation (QCR), is an

extension of the eddy-viscosity hypothesis that includes quadratic moments of the strain rate and vorticity tensors to introduce anisotropy to the normal turbulent stresses (u'^2, v'^2, w'^2) that are absent from Boussinesq closures. This takes the form

$$\tau_{ij,QCR} = \tau_{ij} - C_{NL1}\left[O_{ik}\tau_{jk} + O_{jk}\tau_{ik}\right] \tag{1}$$

where

$$\tau_{ij} = 2\mu_t\left(S_{ij} - \frac{1}{3}\frac{\partial u_k}{\partial x_k}\right) \tag{2}$$

and

$$O_{ik} = \frac{\left(\dfrac{\partial u_i}{\partial x_k} - \dfrac{\partial u_k}{\partial x_i}\right)}{\sqrt{\dfrac{\partial u_m}{\partial x_n}\dfrac{\partial u_m}{\partial x_n}}} \tag{3}$$

The value of C_{NL1} in Eq. 1 is generally set to 0.30, and promotes the canonical 4:2:3 behavior of the normal stresses in two-dimensional planar shear layers[8]. Use of QCR has been demonstrated to improve solution robustness and accuracy in wing-body juncture flows, particularly in the presence of incipient separation[9,27].

IV. Results and Discussion

Various solution strategies and turbulence modeling combinations were employed with the three CFD codes, and these are summarized below in Table 5. The ID and Datset Name are used in subsequent results, and the Dataset Name is formatted as "Solver-Discretization-TurbulenceModel-QCR-GridSystem". For example, a 2nd-order central difference solution obtained on the Standard Overset grid system using OVERFLOW with the SARC turbulence model variant and without the QCR option is referred to as "OF-cen2-SARC-noQCR-SO".

Table 5. Description of solution datasets.

ID	Dataset Name	Organization	Code	Spatial Discretization	Turbulence Model	QCR	Grid Type
q	OF-cen2-SARC-noQCR-SO	Boeing / NASA	OVERFLOW v2.2k	Central, $O(2)$	SA-noft2-RC	No	Standard Overset
r	OF-cen2-SARC-QCR-SO			Central, $O(2)$	SA-noft2-RC	Yes, QCR2000	Standard Overset
o	OF-upw3-SARC-QCR-SO	Penn State Applied Research Lab	OVERFLOW v2.2l	Upwind, $O(3)$	SA-noft2-RC	Yes, QCR2000	Standard Overset
p	OF-weno5-SARC-QCR-SO			WENO, $O(5)$	SA-noft2-RC	Yes, QCR2000	Standard Overset
a	AD-cen2-SA-noQCR-MO	University of Michigan	ADflow	Central, $O(2)$	SA-noft2	No	Modified Overset
b	AD-cen2-SA-noQCR-MB			Central, $O(2)$	SA-noft2	No	Multi-Block
c	AD-cen2-SA-QCR-MB			Central, $O(2)$	SA-noft2	Yes	Multi-Block
e	eA-cen2-SA-noQCR-SO	ONERA	elsA	Central, $O(2)$	SA	No	Standard Overset
f	eA-cen2-SA-QCR-SO			Central, $O(2)$	SA	Yes, QCR2000	Standard Overset

A. CRM Nacelle-Pylon Drag Increment

The WB and WBNP grid-convergence study results of all datasets for drag (total, skin-friction, pressure, and increment), pitching-moment, and angle of attack for $C_L = 0.5$ are plotted in Fig. 8. Total drag values for all solutions are converging to limits between 253 and 255 counts for the WB configuration and between 275-277 counts for the WBNP configuration. The predicted nacelle-pylon drag increment for the OVERFLOW solutions is 21-22 counts, whereas ADflow predicts a larger increment of nearly 23 counts. elsA predicts a value just above 22 counts, which is lower than ADflow but higher than OVERFLOW. Pressure and skin-friction drag components show distinct trends across the solvers. OVERFLOW predicts higher pressure drag than ADflow and elsA for the grid levels considered; however, extrapolating the values to the continuum limit shows the data to be grouped based

on whether or not QCR is used. The solutions without QCR predict lower skin-friction drag than those with QCR. Skin-friction drag predictions exhibit two bands: solutions that used OVERFLOW and solutions that did not. Non-OVERFLOW solutions have higher skin-friction drag, and while they did not use QCR, the OVERFLOW values without QCR are more similar to the other OVERFLOW predictions than with the other non-QCR results. Two other factors are also at play between the two groups: the use of the 'RC' correction and the solvers being cell-centered versus node-centered.

Predictions for the pitching-moment coefficient are scattered across the various datasets, with the strongest agreement being between the three OVERFLOW solutions with SARC and QCR but with different discretizations. The increase in nose-down moment due to the nacelle-pylon is consistent across all datasets. The angle of attack for C_L = 0.5 exhibits groupings similar to what was observed for the skin-friction coefficient; however, the OVERFLOW solutions without QCR lies distinctly in between the other OVERFLOW data and the elsA/ADflow data. It may then be inferred that the 'RC' correction and QCR each alter the angle by approximately 0.05° for both the WB and WBNP configurations.

Predicted wing surface pressures for the WB and WBNP configurations are compared in Fig. 9 for all three codes. To provide an appropriate comparison, the plotted solutions represent the use of a 2nd-order central difference scheme without the QCR option. There is very strong agreement between the three codes at all spanwise stations for both configurations. The characteristics of the pressure distributions, including the upper-surface shockwave location, are consistently predicted across the codes. There is some scatter in the details of the shockwave, such as minimum pressure and total pressure rise; however, there appear to be no trends based on the use of the RC correction or the use of standard versus modified overset grids.

Detailed investigation of the predicted flow fields revealed some inconsistencies across the various solutions in the structure of the shockwave near the tip. An additional weak compression shock appears near the leading edge in this region, giving the shock a lambda-like shape on the surface. A comparison of the pressure distributions at the η = 0.950 station is plotted in Fig. 10 for the solvers at multiple grid refinement levels (only the L3 solution was available for the OF-upw3-SARC-QCR-SO dataset). For the various central-difference solutions, the location of the primary shockwave does not change as the grid is refined, but the shockwave does sharpen. Refining the grid reveals the presence of a weaker compression around x/c = 0.20, upstream of the main shock. The upwinded solution, however, predicts this compression to be stronger and more distinct. There are numerous possible explanations for the discrepancy in solution behavior, such as upwinding strategy and order of accuracy, and as such, it is the subject of ongoing investigation.

B. CRM WB Static Aero-Elastic Effect (Buffet Study)

An angle-of-attack sweep ranging from 2.5° to 4.0° in quarter-degree increments (7 total angles) was performed using all codes. The grids for each angle of attack were generated based on the measured aero-elastic deformation (bending and twist) from the wind-tunnel tests for the same angles. Polars of the predicted aerodynamic forces and moments are plotted in Fig. 11. As the total drag coefficient includes strong lift-dependent component that obscures solver-specific behaviors, an idealized vortex-induced drag component has been subtracted to provide a pseudo-profile-drag coefficient in the figure.

The various lift curves show distinct banding between the different solution approaches, and this is consistent with the previously described behavior for the predicted angle of attack. While the trim cases focused on desired lift coefficient, this study is looking at the behavior at specific angles of attack. All QCR-based solutions show similar lift behavior across the angle of attack range, whereas two of the non-QCR datasets exhibit breaks in the lift curve corresponding to the buffet boundary. These breaks in the lift curve correspond with rapid growth of the side-of-body separation bubble in the wing-body juncture and its interaction with the primary shockwave on the wing. The non-QCR ADflow solutions show a strong dependency on the grid topology. Surface streamlines in the wing-body juncture for the non-QCR ADflow solutions on both the Modified Overset and Multiblock grid systems are shown in Fig. 12. The solutions on the Modified Overset grid exhibit a smaller bubble, and thus no lift break in this angle of attack range, whereas the Multiblock solution (with the same surface grids) shows a sharp break between 3.25° and 3.5°. The volume grids in this region have differing topologies between the mesh systems, which may be a contributing factor in the drastically different behavior due to the different viscous differencing directions and grid skew. The behavior of the SA model without QCR is known to be inconsistent in juncture flow regions, even for unstructured grids[28], so the possibility of multiple solutions to the governing equations must be considered.

All of the QCR-based solutons on the Standard Overset meshes (using OVERFLOW and elsA) show strong agreement in the pseudo-profile-drag polar, whereas the QCR-based solutions from ADflow on the multiblock grid exhibits lower drag at the higher angles of attack. The non-QCR solutions exhibit lower drag values than their QCR

counterparts for pre-buffet angles of attack. For the pitching-moment coefficient, all QCR-based solutions exhibit less nose-down moment than the non-QCR solutions, and of those, the non-SARC results show greater nose-down moment than the SARC results.

C. CRM WB Grid Adaptation

A solution adaption capability for both the Cartesian off-body regions and for curvilinear near-body grids has been implemented in the OVERFLOW overset grid computational fluid dynamics code[29,30]. The adaption capability in OVERFLOW is considered a feature-based process, which does well for hard flow features (e.g. shocks, wakes, and vortices), but is not an output-based or adjoint error-based approach. Building on the Cartesian off-body approach inherent in OVERFLOW and the original adaptive refinement method developed by Meakin[31], the off-body adaption provides for automated creation of multiple levels of finer Cartesian off-body grids. The near-body approach follows closely that used for the Cartesian off-body grids, but inserts refined grids in the computational space of original near-body grids. Refined curvilinear grids are generated using parametric cubic interpolation, with one-sided biasing based on curvature and stretching ratio of the original grid. Sensor functions, grid marking, and solution interpolation tasks are implemented in a consistent and efficient way for both the off-body and near-body grids. Refinement is based on normalized second-undivided differences of the flow variables. A goal-oriented procedure, based on largest error first, is included for controlling growth rate and maximum size of the adapted grid system. The adaption process is almost entirely parallelized using MPI, resulting in a capability suitable for viscous, moving body simulations. Two- and three-dimensional examples are presented. Coupled with load-balancing and an in-memory solution interpolation procedure, the adaption process provides very good performance for steady-state and time-accurate simulations on parallel computing platforms.

For the off-body Cartesian adaption process[29], within the original off-body regions, a cube or "box" of points (e.g., 8 x 8 x 8 points) is examined and if any point is marked for refinement, the box is flagged for refinement. Alternatively, if all points are marked for coarsening, the box is flagged for coarsening. If the box is not flagged for refinement or coarsening, it is left at the current refinement level. In the current implementation, grid regions can only coarsen or refine by one grid level at a time. These coarsening and refinement boxes are then used in the off-body Cartesian grid generation process to create a new adapted grid system.

For the near-body grids, several steps are involved in the adaption process[30]. First, an error estimate or sensor function is computed as a field quantity. This function must be converted to a marker function that indicates what parts of the grid should be refined or coarsened. This marker function is further adjusted to satisfy a limit on global grid size. Next, the new grid system is created, with refined near-body grids preserving the smoothness and geometry features of the original grids. Finally, the flow solution is interpolated from the old grid system to the new system.

OVERFLOW's adaption process was applied to the L2-coarse wing-body grid defined above. The original L2-coarse grid near body system was modified for use with the adaption process and the connectivity was switched from a Pegasus based approach to the DCF approach (which required the development of a set of XRAYs). All periodic meshes were broken into overlapping grids (OVERFLOW's adaption cannot be applied to grids with a periodic boundary condition) and the off-body Cartesian boxes were removed. All near-body surface grids, in particular grid point distribution, were maintained. The total grid size for the new coarse grid is 14.4 million (M) points with 50.3 thousand (K) wing surface points. The new coarse grid case was converged to the same level as the original L2-coarse grid system, labeled Case B below.

Two results from adaption are presented here. In the first case, 2 levels of near-body adaption were applied to the upper surface of the wing only along with 3 levels of off-body adaption (principally to enhance the capture of the wakes and tip vortices). The total number of grid points was restricted through the goal-oriented procedure to 100M points, the resulting adapted grid has 98.3 M total points and 387.6K wing surface points. Results for this case are labeled C in Table 6. In the second case, first we adapt 1 level for both the near-body and off-body grids, then uniformly refine the upper wing grid to 2 levels to give a better base for the final 3 levels of near-body and 2 levels of off-body grid adaption. This result is labeled D in Table 6. The total number of grid points was restricted through the goal-oriented procedure to 400M points, the resulting adapted grid has 388.9M total points and 895.1K wing surface points as shown in Table 6 below. The solution for the L6-ufine grid is used for reference and is labeled A below This grid has 82.8M points and 156.3K wing surface points.

Table 6. OVERFLOW adapted grid parameters.

Case	Initial Grid	Phase	Type	Region	Limit	NB Levels	OB Levels	Total Points	Increase	WingSrf Points	Increase
A	L6, ufine	n/a	none	n/a	n/a	n/a	n/a	82.8M		156.3K	
B	L2, coarse	n/a	none	n/a	n/a	n/a	n/a	14.4M		50.3K	
C	L2, coarse	1	gradient	wing, wake	100M	3	2 (wake)	98.3M	6.8x	387.6K	7.7x
D	L2, coarse	1	uniform	all zones	n/a	1	1				
		2	uniform	wing	n/a	2	0				
		3	gradient	wing, body	400M	3	2	388.9M	27x	895.1K	17.8x

Notes:
> existing near-field and far-field box grids were used
> gradient-based adaption used undivided 2nd difference for sensor function
> NB = near-body, OB = off-body

Figure 13 shows total computed drag from the adaption cases compared to the grid family results obtained via uniform refinement. The variable (S) plotted along the horizontal axis is the total number of surface grid points. Since this is a 2D evaluation of grid refinement, the power S is raised to is 2/2 instead of 2/3 for 3D. The new coarse grid (DCF mode) result, labeled B in Figure 13, is less than 1 count higher than the original coarse grid (Pegasus mode) result due to the differences in connectivity and grid topology. The two adaptive cases (C and D) fall to the left of the L6-ufine case (A) due to increased grid count with the adapted case D falling along the asymptotic convergence of grid refinement. Solver convergence was considered good with adaption turned on where multi-grid was shut off and 50 iterations was run between adaption cycles.

Figure 14 shows comparisons of the C_p at various wing stations, which highlights the improvement in the shock resolution with both increasing grid size and the adaption process. The effect of the adaption on the shock structure is clearly evident in the adapted cases, especially case D where the tip shock region shows a well resolved lambda shape, and is more similar to what had been observed in the upwinded MUSCL solution (Fig. 10). The tip region is further explored in Figures 15 and 16, which show grid resolution and pressure contours for the four cases defined in Table 6. Figure 17 shows a comparison with experimental data[5], with the various cases. The slight compression and expansion at about 20% chord at this station is evident in both the experimental data and the adapted case D.

American Institute of Aeronautics and Astronautics

Figure 8. Effect of grid resolution on predicted aerodynamic forces and moments of WB and WBNP configurations.

American Institute of Aeronautics and Astronautics
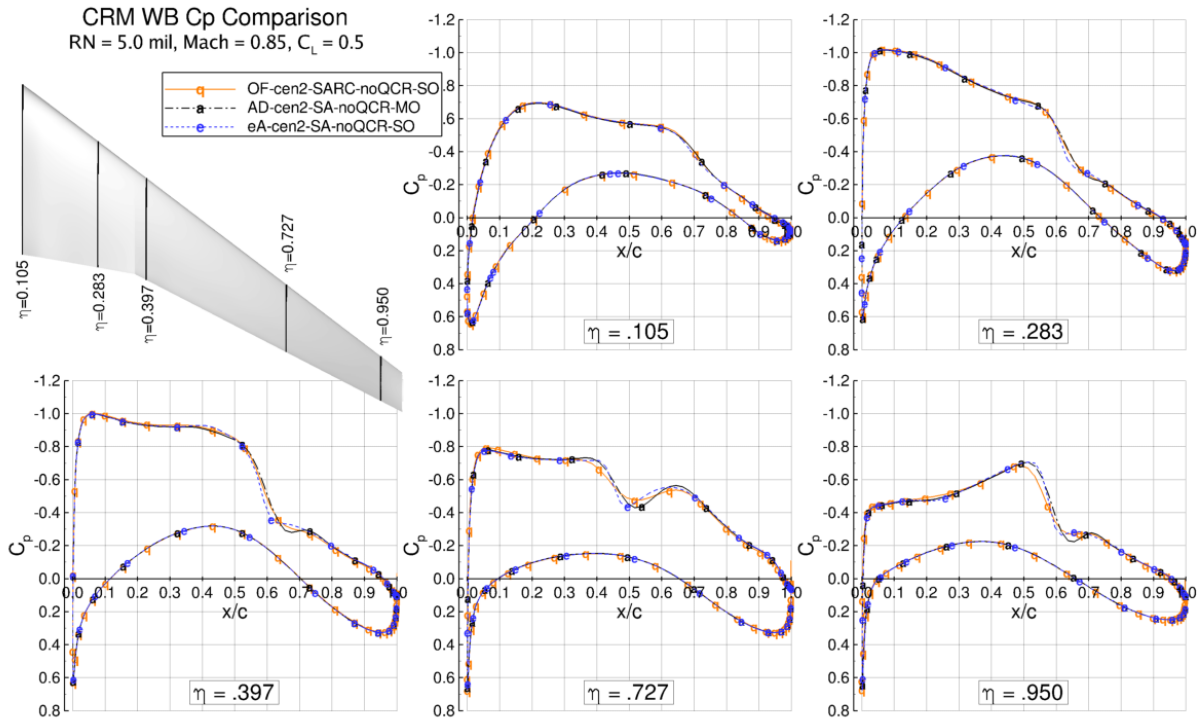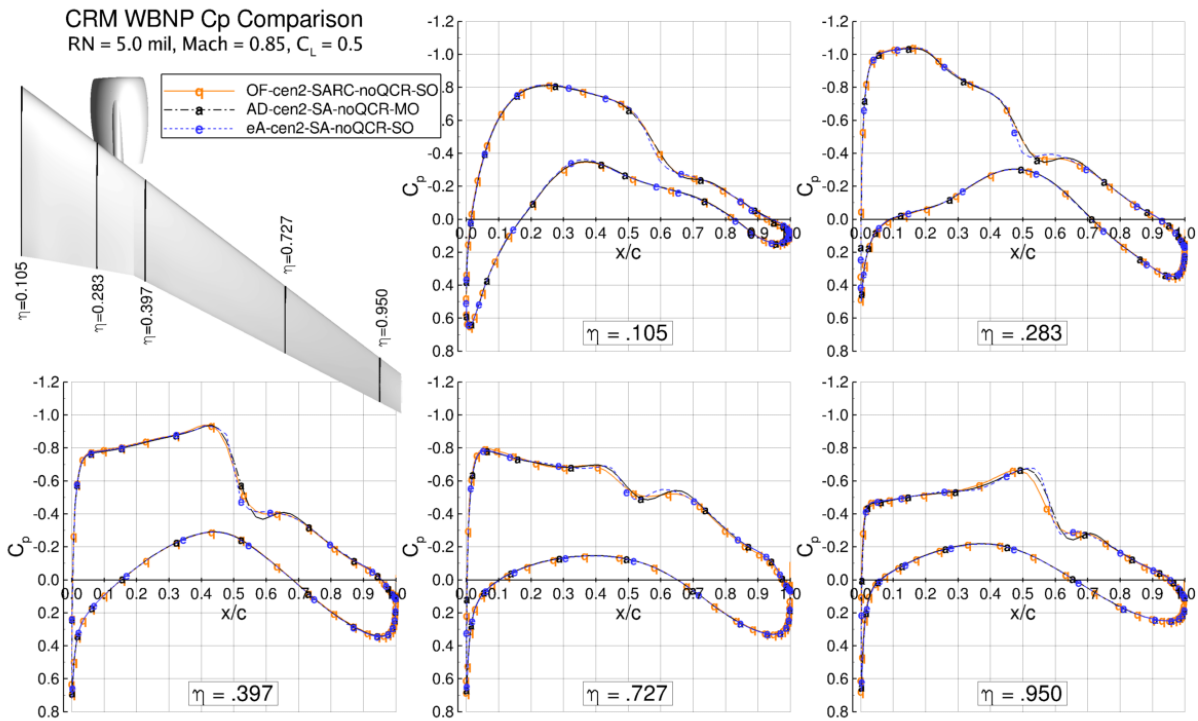
(a) WB configuration

(b) WBNP configuration

Figure 9. Predicted surface pressure distributions at select spanwise locations of the WB and WBNP configurations.
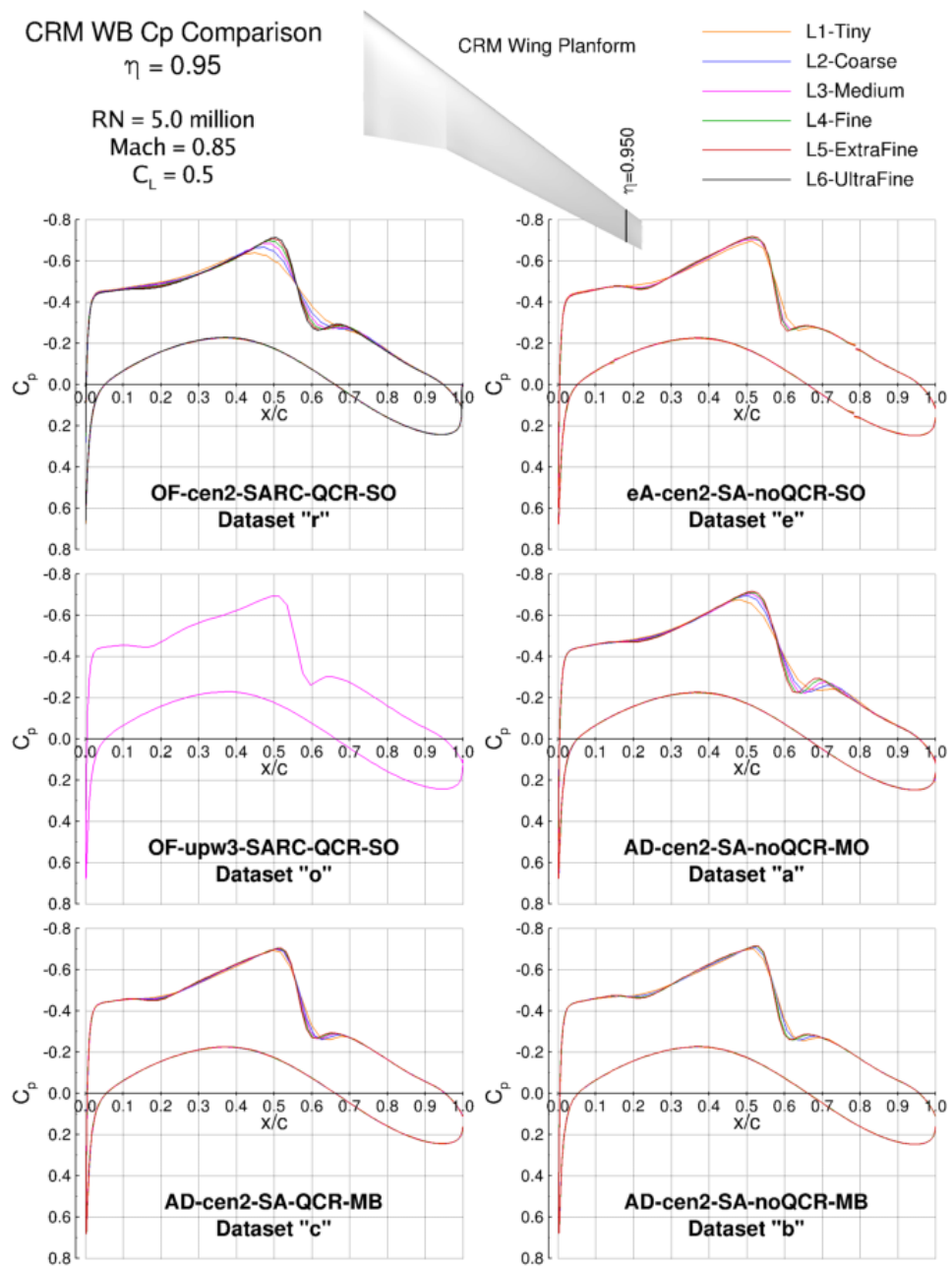
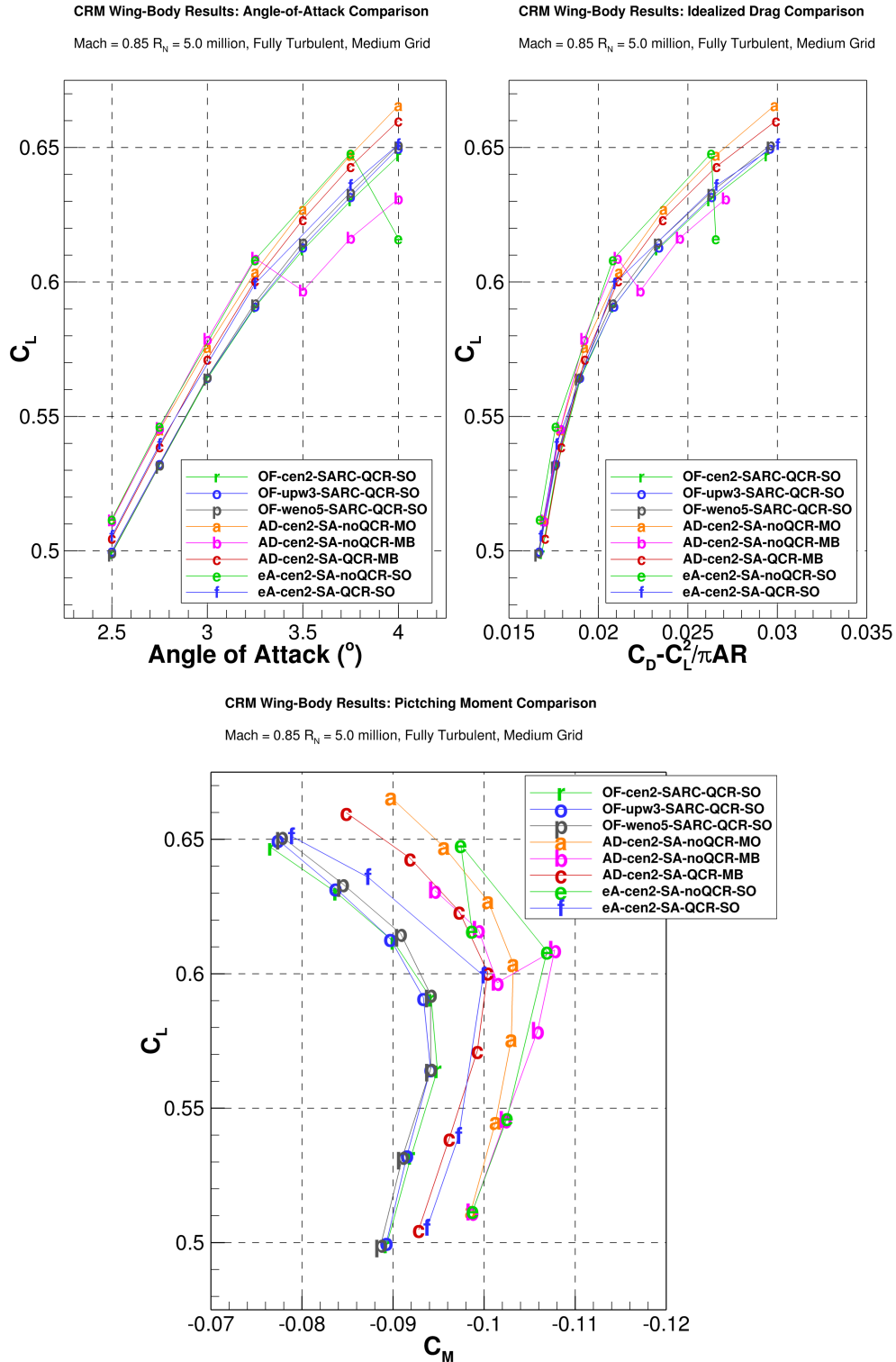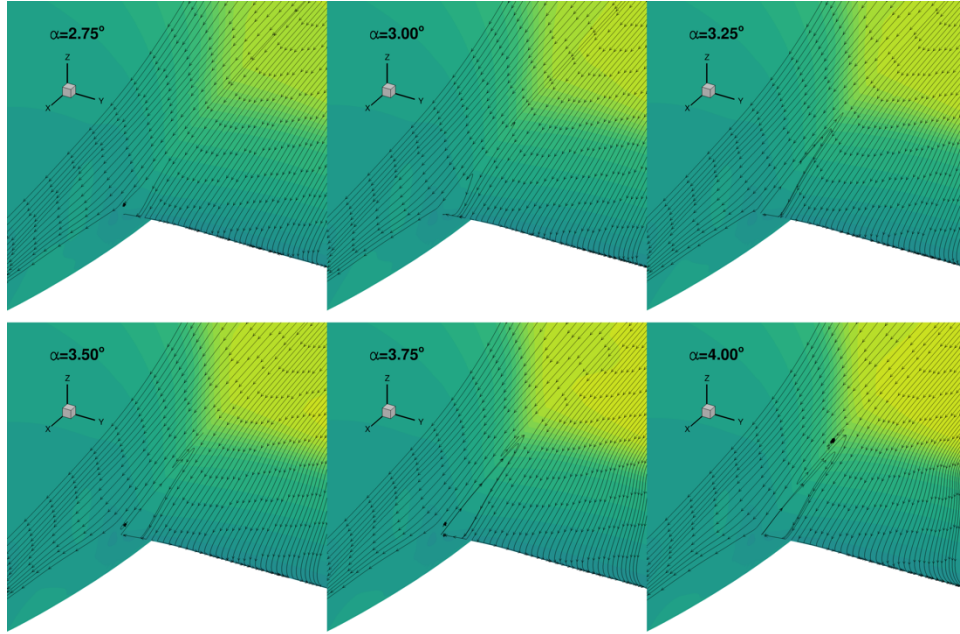**Figure 10. Surface pressure distributions at $\eta = 0.95$, including the effect of grid resolution and discretization.**
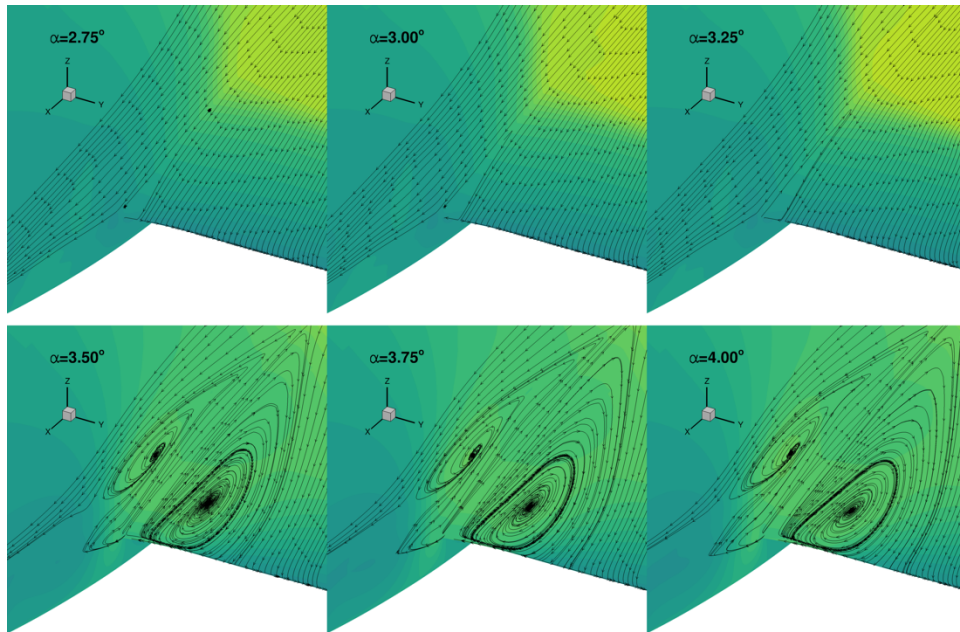
CRM Wing-Body Results: Angle-of-Attack Comparison

Mach = 0.85 R_N = 5.0 million, Fully Turbulent, Medium Grid

CRM Wing-Body Results: Idealized Drag Comparison

Mach = 0.85 R_N = 5.0 million, Fully Turbulent, Medium Grid

CRM Wing-Body Results: Pictching Moment Comparison

Mach = 0.85 R_N = 5.0 million, Fully Turbulent, Medium Grid

Figure 11. Aerodynamic characteristics of WB configuration through an alpha sweep.

American Institute of Aeronautics and Astronautics

(a) Modified Overset grid

(b) Multiblock grid

Figure 12. Effect of grid topology on predicted side-of-body separation using ADflow without QCR.
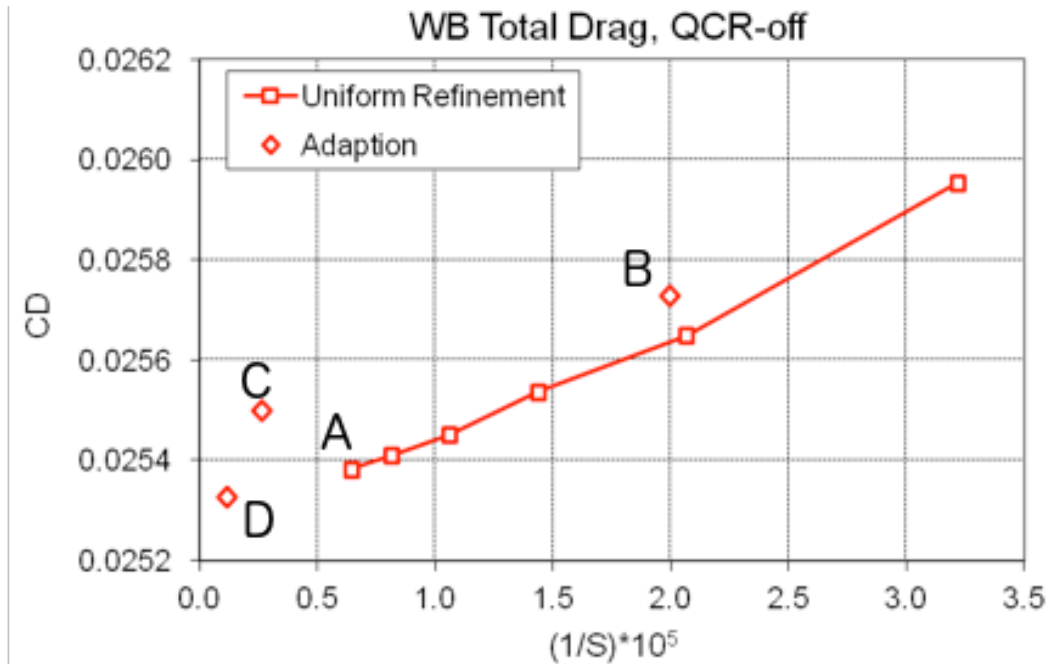
Figure 13. Total drag grid convergence with adaptive results.
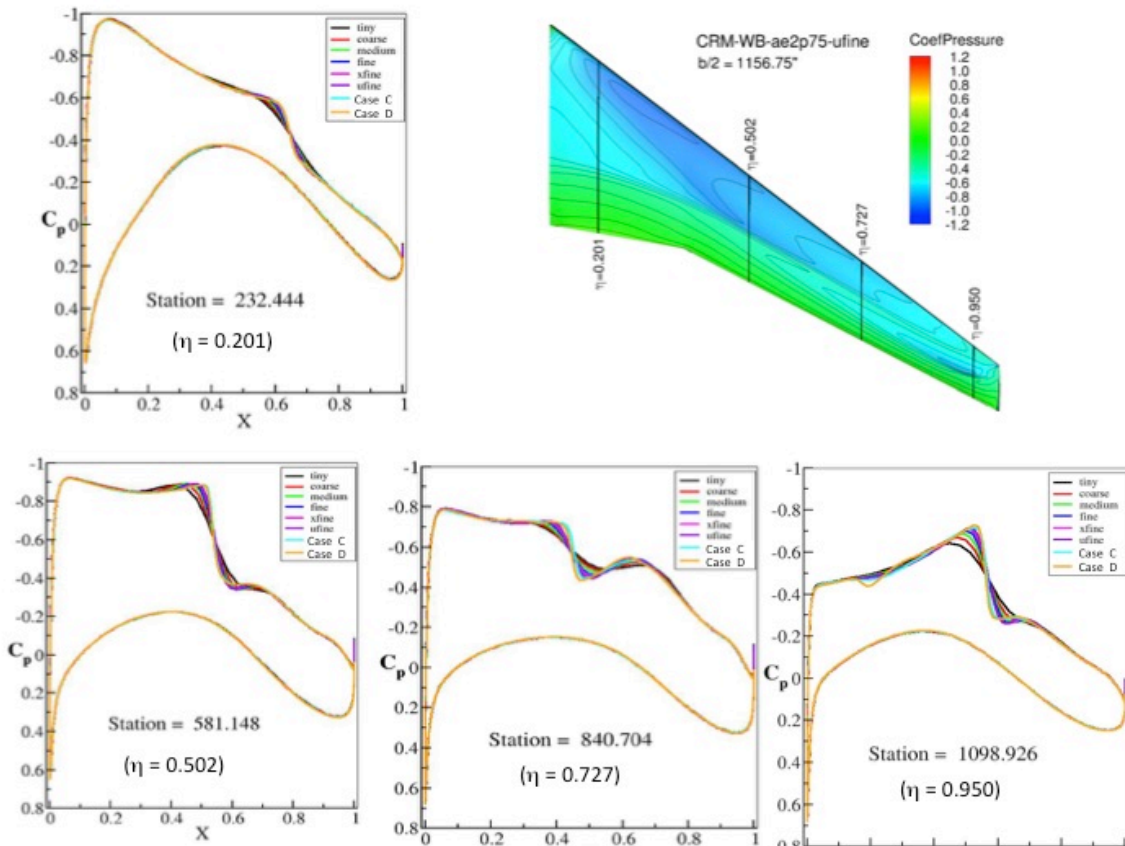
Figure 14. Pressure coefficient comparisons at multiple spanwise wing stations.
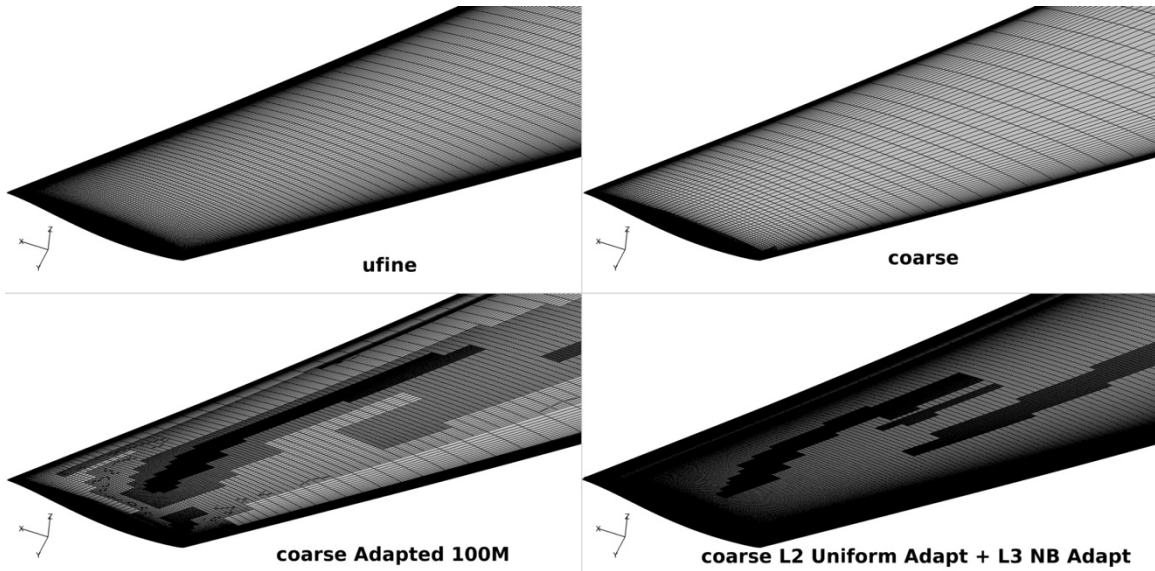
American Institute of Aeronautics and Astronautics

Figure 15. Effect of adaptation of wing surface grid resolution.
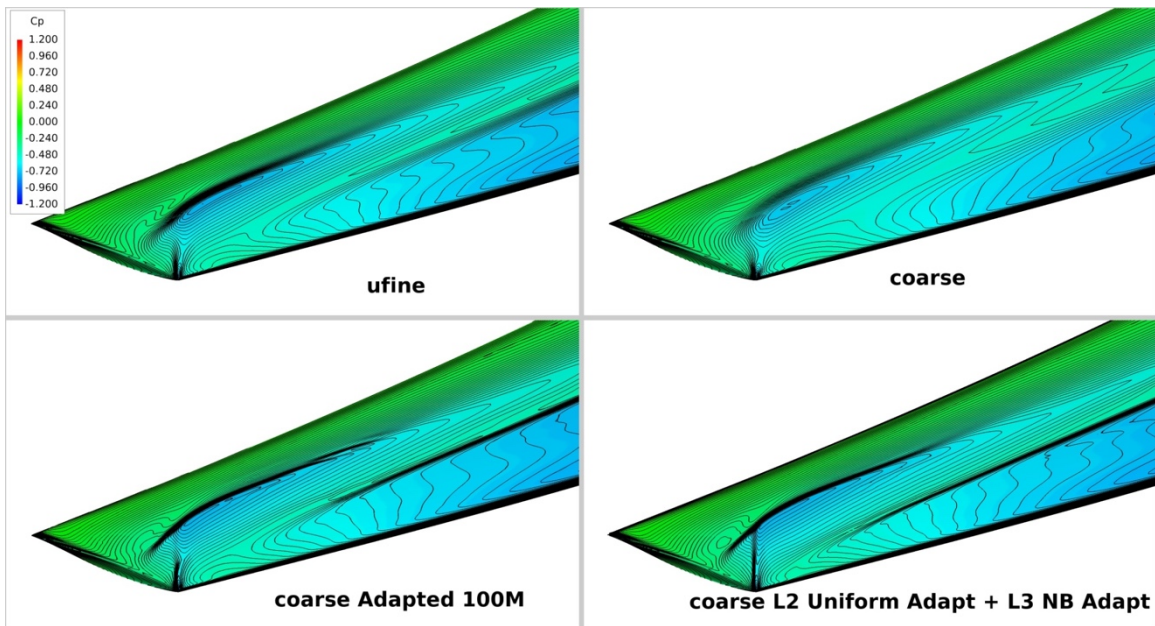
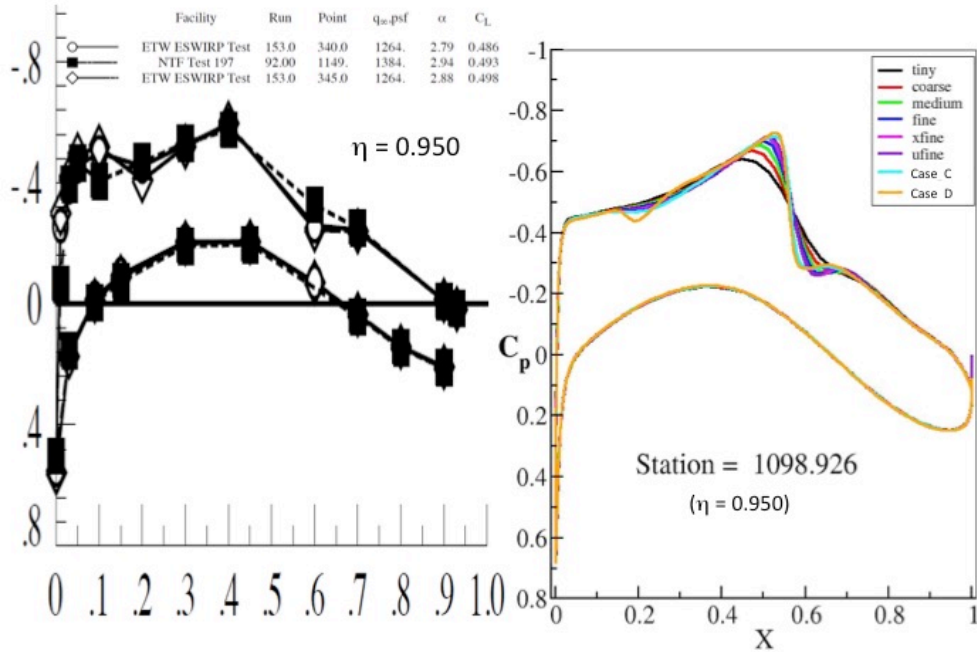**Figure 16. Effect of adaptation and wing-tip region surface pressure coefficient behavior.**

Figure 17. Comparison at outboard station between experiment[5], grid family, and adapted results.

V. Conclusion

Predictions obtained using the OVERFLOW, elsA, and ADflow structured, overset flow solvers for the 6th AIAA Drag Prediction Workshop were compared for the nacelle-pylon drag increment and the angle-of-attack sweep. Results were fairly consistent across all solvers, with the prominent differences attributable primarily to the turbulence modeling strategies employed (i.e. SA vs. SARC, QCR vs. non-QCR) and, to a lesser extent, discretization. Some influence of the discretization scheme was observed in the predicted shock structure near the tip. The upwinded MUSCL scheme predicts a more distinct upstream compression compared to the central-difference solutions. Feature-based grid adaption of a central-difference solution responded to this shock, refining the mesh in its vicinity and providing clear resolution of the compression.

Acknowledgments

References

[1]Tinoco, E. N., Brodersen, O., Keye, S., and Laflin, K., "Summary of Data from the Sixth AIAA CFD Drag Prediction Workshop: CRM Cases 2 to 5," 55th AIAA Aerospace Sciences Meeting, *Abstract accepted*, Grapevine, TX, January 2017.

[2]Vassberg, J. C., Dehaan, M. A., Rivers, M., and Wahls, R. A., "Development of a Common Research Model for Applied CFD Validation Studies," 26th AIAA Applied Aerodynamics Conference, AIAA Paper 2008-6919, Honolulu, HI, August 2008.

[3]Vassberg, J. C. et al., "Summary of the Fourth AIAA Computational Fluid Dynamics Drag Prediction Workshop," *Journal of Aircraft*, Vol. 51, No. 4, 2014, pp. 1070-1089.

[4]Levy, D. W. et al., "Summary of Data from the Fifth AIAA Computational Fluid Dynamics Drag Prediction Workshop," *Journal of Aircraft*, Vol. 51, No. 4, 2014, pp. 1194-1213.

[5]Rivers, M. B. and Dittberner, A., "Experimental Investigations of the NASA Common Research Model in the NASA Langley National Transonic Facility and NASA Ames 11-Ft Transonic Wind Tunnel (Invited)," 49th AIAA Aerospace Sciences Meeting, AIAA Paper 2011-1126, Orlando, FL, January 2011.

[6]Rumsey, C. L., Smith, B. R., Huang, G. P., "Description of a Website Resource for Turbulence Modeling Verification and Validation," 40th AIAA Fluid Dynamics Conference and Exhibit, AIAA Paper 2010-4742, Chicago, IL, June-July 2010.

[7]Nichols, R. H. and Buning, P. G., "User's Manual for OVERFLOW 2.2," NASA Langley Research Center, Hampton, VA, Aug. 2010.

[8]Spalart, P. R., "Strategies for Turbulence Modelling and Simulation," *International Journal of Heat and Fluid Flow*, Vol. 21, 2000, pp. 252-263.

[9]Sclafani, A. J., Vassberg, J. C., Winkler, C., Dorgan, A. J., Mani, M., Olsen, M. E., and Coder, J. G., "Analysis of the Common Research Model Using Structured and Unstructured Meshes," *Journal of Aircraft*, Vol. 51, No. 4., 2014, pp. 1223-1243.

[10]Spalart, P. R. and Allmaras, S. R., "A One-Equation Turbulence Model for Aerodynamic Flows," *Recherche Aerospatiale*, No. 1, 1994, pp. 5-21.

[11]Shur, M. L., Strelets, M. K., Travin, A. K., and Spalart, P. R., "Turbulence Modeling in Rotating and Curved Channels: Assessing the Spalart-Shur Correction," *AIAA Journal*, Vol. 38, No. 5, 2000, pp. 784-792.

[12]Jameson, A., Schmidt, W., and Turkel, E., "Numerical Solution of the Euler Equations by Finite Volume Methods Using Runge Kutta Time Stepping Schemes," 14th Fluid and Plasma Dynamics Conference, AIAA Paper 1981-1259, Palo Alto, CA, 1981.

[13]Hue, D., Chanzy, Q., and Landier, S., "DPW-6: Drag Analyses and Increments Using Different Geometries of the CRM Airliner," *Submitted to Journal of Aircraft*, 2016.

[14]Van der Weide, E., Kalitzin, G., Schluter, J., and Alonso, J. J., "Unsteady Turbomachinery Computations Using Massively Parallel Platforms," 44th AIAA Aerospace Sciences Meeting, AIAA Paper 2006-0421, Reno, NV, January 2006.

[15]Mader, C. A., Martins, J. R. R. A., Alonso, J. J., and van der Weide, E., "ADjoint: An Approach for the Rapid Development of Discrete Adjoint Solvers," *AIAA Journal*, Vol. 46, No. 4, 2008, pp. 863-873.

[16]Lyu, Z., Kenway, G. K., Paige, C., and Martins, J. R. R. A., "Automatic Differentiation Adjoint of the Reynolds-Averaged Navier-Stokes Equations with a Turbulence Model," 21st AIAA Computational Fluid Dynamics Conference, AIAA Paper 2013-2581, San Diego, CA, June 2013.

[17]Lyu, Z., Kenway, G. K., and Martins, J. R. R. A., "Aerodynamics Shape Optimization Investigations of the Common Research Model Wing Benchmark," *AIAA Journal*, Vol. 53, No. 4, 2015, pp. 968-985.

[18]Lyu, Z. and Martins, J. R. R. A., "Aerodynamic Design Optimization Studies of a Blended-Wing-Body Aircraft," *Journal of Aircraft*, Vol. 51, No. 5, pp. 1605-1617.

[19]Chen, S., Lyu, Z., Kenway, G. K. W., and Martins, J. R. R. A., "Aerodynamic Shape Optimization of the Common Research Model Wing-Body-Tail Configuration," *Journal of Aircraft*, Vol. 53, No. 1, 2016, pp. 276-293.

[20]Kenway, G. K. W, "Multipoint Aerodynamic Shape Optimization Investigations of the Common Research Model Wing," *AIAA Journal*, Vol. 54, No. 1, 2016, pp. 113-128.

[21]Kenway, G. K. W., Kennedy, G. J., and Martins, J. R. R. A., "Scalable Parallel Approach for High-Fidelity Steady-State Aeroelastic Analysis and Derivative Computations," *AIAA Journal*, Vol. 52, No. 5, 2014, pp. 935-951.

[22]Kenway, G. K. W. and Martins, J. R. R. A., "Multipoint High-Fidelity Aerostructural Optimization of a Transport Aircraft Configuration," *Journal of Aircraft*, Vol. 51, No. 1, 2014, pp. 144-160.

[23]Landmann, B. and Motagnac, M., "A highly automated parallel Chimera method for overset grids based on the implicit hole cutting technique," *Journal for Numerical Methods in Fluids*, Vol. 66, 2011, pp. 778-804.

[24]Chan, W. M., "Enhancements to the Hybrid Mesh Approach to Surface Loads Integration on Overset Structured Grids," 19th AIAA Computational Fluid Dynamics Conference, AIAA Paper 2009-3990, San Antonio, TX, June 2009.

[25]"ANSYS ICEM CFD 15.0," ANSYS, Inc., Canonsburg, PA, November 2013.

[26]Chan, W. M., Rogers, S. E., Pandya, S. A., Kao, D. L., Buning, P. G., Meakin, R. L., Boger, D. A., and Nash, S. M., "Chimera Grid Tools User's Manual, Version 2.1," Moffett Field, CA, 2010.

[27]Yamamoto, K., Tanaka, K., Murayama, M., "Effect of a Nonlinear Constitutive Relation for Turbulence Modeling on Predicting Flow Separation at Wing-Body Juncture of Transonic Commercial Aircraft," 30th AIAA Applied Aerodynamics Conference, AIAA Paper 2012-2895, New Orleans, LA, June 2012.

[28]Park, M. A, Laflin, K. R., Chaffin, M. S., Powell, N., and Levy, D. W., "CFL3D, FUN3D, and NSU3D Contributions to the Fifth Drag Prediction Workshop," *Journal of Aircraft*, Vol. 51, No. 4, 2014, pp. 1268-1283.

[29]Buning, P. G. and Pulliam, T. H., "Cartesian Off-Body Grid Adaption for Viscous Time-Accurate Flow Simulations," 20th AIAA Computational Fluid Dynamics Conference, AIAA Paper 2011-3693, Honolulu, HI, June 2011.

[30]Buning, P. G. and Pulliam, T. H., "Near-Body Grid Adaption for Overset Grids," 46th AIAA Fluid Dynamics Conference, AIAA Paper 2016-3326, Washington, DC, June 2016.

[31]Meakin, R. L., "An Efficient Means of Adaptive Refinement Within Systems of Overset Grids," 12th AIAA Computational Fluid Dynamics Conference, AIAA Paper 1995-1722, San Diego, CA, June 1995.